Advanced Energy Materials

ADVANCED ENERGY MATERIALS
www.advenergymat.de

RESEARCH ARTICLE OPEN ACCESS

Depth-of-Discharge-Dependent Chemical Evolution in Sulfurized Polyacrylonitrile Cathodes for Ether-Based Room-Temperature Sodium–Sulfur Batteries

Liwen Yang[1] | Angelina Sarapulova[2,3] | Bercis Pektas[4,5] | Rong Li[6] | Hatice Mutlu[4,5,7] | Sonia Dsoke[2,3,8]

[1]Institute for Applied Materials (IAM), Karlsruhe Institute of Technology (KIT), Eggenstein-Leopoldshafen, Germany | [2]Fraunhofer Institute for Solar Energy Systems, Freiburg, Germany | [3]FMF-Freiburg Materials Research Center, University of Freiburg, Freiburg, Germany | [4]Mulhouse Materials Science Institute (IS2M), University of Mulhouse, Mulhouse cedex, France | [5]Department of Chemistry, Technical Polymer Chemistry, Rheinland-Pfälzische Technische Universität Kaiserslautern-Landau (RPTU), Kaiserslautern, Germany | [6]School of Chemistry and Chemical Engineering, Guizhou University, West Campus of Guizhou University, Guiyang, China | [7]Leibniz-Institut für Verbundwerkstoffe GmbH (IVW), Kaiserslautern, Germany | [8]Institute for Sustainable Systems Engineering (INATECH), University of Freiburg, Freiburg, Germany

Correspondence: Rong Li (lir@gzu.edu.cn) | Hatice Mutlu (hatice.mutlu@rptu.de) | Sonia Dsoke (sonia.dsoke@ise.fraunhofer.de)

Received: 16 December 2025 | **Revised:** 23 February 2026 | **Accepted:** 2 March 2026

Keywords: deep discharge | different depths of discharge | room temperature Na–S batteries | structure change

ABSTRACT

Room-temperature sodium–sulfur (RT Na–S) batteries are emerging as promising next-generation energy storage systems owing to their high theoretical capacity and environmental friendliness. Nevertheless, the intrinsic insulating nature of elemental sulfur and the polysulfide shuttle effect significantly limit the widespread practical and large-scale applications of RT Na–S batteries. Sulfurized polyacrylonitrile (SPAN) is a potential cathode candidate for Na–S batteries, which provides efficient charge transfer due to the conjugated structure of SPAN and avoids the formation of long-chain polysulfide by its structure that only has a short sulfur–sulfur chain. However, the decay mechanism of the SPAN positive electrode in ether-based electrolyte RT Na–S batteries remains poorly understood. In this study, SPAN was studied as a cathode material in ether-based RT Na–S cells. The focus was on the structural evolution of the material during the first few cycles and on variations at different depths of discharge (DOD). This work reveals that deep discharge below 1.0 V affects the structure of SPAN, the equilibrium of polysulfides in the electrolyte, and the growth of sodium dendrites at the negative electrode. On this basis, to enhance the cycling stability and rate performance, carbon-coated functionalized separators are incorporated in the cell.

1 | Introduction

Nowadays, energy has become an urgent global concern. The next round of a high-quality and sustainable global economy is based on the premise of reasonably addressing climate challenges and steering energy conversion and storage toward green, low-carbon solutions [1]. "Carbon neutrality" has emerged as a central goal of energy planning worldwide [2]. In addition to intermittent energy sources, such as wind and solar energy, the integration of secondary batteries as a sustainable and stable energy storage system is an inevitable requirement [3]. At the same time, the development of electric vehicles requires batteries with higher energy and improved sustainability. Indeed, rechargeable batteries play a crucial role in the transformation of traditional energy infrastructure into new, cleaner energy systems [4].

Room-temperature sodium–sulfur (RT Na–S) batteries, particularly those with ether-based electrolytes, are an area of active

research as they offer the potential to operate at ambient temperatures, unlike traditional high-temperature Na–S batteries [5]. RT Na–S batteries leverage the properties of ether-based electrolytes, such as tetraethylene glycol dimethyl ether (TEGDME) or 1,3-dioxolane, for lower-temperature operation. These electrolytes can generate dense solid electrolyte interphase (SEI) layers for sodium metal anodes, achieving enhanced cycling stability compared to ester-based electrolytes [6]. However, RT Na–S batteries are still at their early stage of development and still face a number of challenges that hinder their practical application. [7] Compared with lithium–sulfur batteries, sodium sulfur batteries produce sodium polysulfide with higher solubility in the electrolyte, which can diffuse to the sodium metal anode side to cause more severe "shuttle effect" and result in stronger capacity fading. Meanwhile, sodium polysulfide is thermodynamically more stable than lithium polysulfide, which leads to slower reaction kinetics. The sodium anode suffers from a less stable solid–electrolyte interphase (SEI) and more pronounced dendritic growth than its lithium counterpart when operated in ether-based electrolytes. The high reactivity between the sodium surface and the electrolyte results in the formation of an SEI of a different nature than the analogue lithium SEI. This fragile SEI layer is prone to breaking down, resulting in continuous side reactions, the sodium dendrite formation, and ultimately a shortened cycle life [8].

This not only leads to self-discharge and low coulombic efficiency, but also causes severe capacity fading over time [9]. Additionally, electrolyte degradation poses a significant barrier to long-term performance. Ether solvents are not entirely stable against reactive sodium polysulfides, and their gradual chemical degradation generates by-products that increase the internal resistance and reduce the cell's long-term stability and performance [10]. Moreover, under high current densities, RT Na–S batteries face additional challenges due to their low ion conductivity, high electrochemical polarization, severe shuttle effect, and rapid growth of sodium dendrites. Altogether, the above challenges lead to low reversible capacity and rapid capacity decay, highlighting the need for improved materials and cell designs to unlock the full potential of RT Na–S battery technologies [11].

Rationale cathode design is crucial to address the above-mentioned challenges [5]. One widely adopted strategy involves engineering porous cathodes or incorporating sulfur into conductive carbon matrices, which can physically anchor polysulfides, thereby reducing their dissolution into the electrolyte and mitigating the shuttle effect [12–14]. Among various sulfur-based cathode materials [15], the sulfurized polyacrylonitrile (SPAN) contains short-chain sulfur species ($S_{2\text{-}3}$) that are covalently bonded to the polyacrylonitrile (PAN) backbone. This short-chain sulfur can effectively prevent the formation of soluble long-chain polysulfides, thereby fundamentally aiding in solving the shuttle effect [16]. In addition, the thermal treatment used during the SPAN synthesis induces partial conjugation along the PAN backbone [17]. This conjugated structure significantly stabilizes the structure of SPAN, transforming it into a better electronic conductor compared to elemental sulfur, which is inherently insulating. Thus, the combination of structural stability and improved conductivity makes SPAN a compelling cathode material for metal-sulfur batteries. However, despite its proven efficacy in Li–S systems and ester-based Na–S batteries [18], the application of SPAN in ether-based electrolyte Na–S batteries remains relatively unexplored, offering an exciting and timely opportunity for research [15]. At the same time, the degradation mechanism of SPAN positive electrode in ether-based electrolyte RT Na–S batteries remains poorly understood. Therefore, it is essential to elucidate the structural and electrochemical changes occurring during the initial charge–discharge cycle of the SPAN cathode, as this understanding can serve as a blueprint for cathode structure design and electrode optimization. Subsequently, in this study, SPAN is used as the cathode material in RT sodium–sulfur battery with ether-based electrolytes (i.e.,1.0 M $NaCF_3SO_3$ in TEGDME) under high current density conditions. The decay mechanism occurring during the initial few cycles is explained. In addition, cycle tests at different depths of discharge and post-mortem studies are conducted to provide insights into the evolution of interfacial reactions within the SPAN-sodium cell. On this basis, to further enhance stability and rate capability, carbon functional separator configurations are explored and evaluated.

2 | Experimental

2.1 | Synthesis of Sulfurized Polyacrylonitrile (SPAN)

In a typical process, excess of elemental sulfur (S_8, Alfa Aesar, 99.98%) and polyacrylonitrile polymer powder (Sigma Aldrich, average M_w = 150 000) were mixed thoroughly in agate mortar with a mass ratio of 10:1. Subsequently, the mixture was hated in a tubular furnace at a ramp rate of 2°C min^{-1} to 270°C and held at that temperature for 6 h under Nitrogen atmosphere. Unreacted elemental sulfur is removed from the nitrogen stream during the cooling process. The dark powder SPAN, approximately 5 g, was obtained upon cooling to 25°C. The sulfur content of SPAN is 44.3% (measured by elemental analysis).

2.2 | Electrodes Preparation

All electrodes were prepared by a classical slurry coating: For SPAN-based cathodes, the active material (SPAN), conductive agent (C65, MTI Corporation), and binder (LA133, MSE Supplies) were mixed in a mass ratio of 60:30:10. The detailed procedure is as follow: The LA133 binder was at first prepared as 3% (mass ratio) solution in a H_2O/ethanol (V: V = 1:1). The SPAN powder and C65 powder was at first mixed in agate mortar for 10 min, then LA133 solution was add into mixed materials. The components were dispersed evenly in a H_2O/ethanol (V:V = 1:1) solution and stirred continuously for 12 h on a magnetic stirrer to obtain a uniform black slurry. This slurry was then coated onto aluminum foil (Haeberle, 30 µm, used as the current collector) using the Doctor Blade technique, with a wet thickness of 200 µm. The coated films were first dried at room temperature until the surface of the coating layer was completely dry; after that, the electrode was dried at 60°C under vacuum for 12 h to further remove any residual solvent. Subsequently, circular electrodes with a diameter of 12 mm were punched from the dried films, yielding a sulfur loading of 0.5 mg ± 0.1 cm^{-2}; SPAN loading was 1.13 mg ± 0.1 cm^{-2}. For comparison, elemental sulfur cathodes were prepared using elemental sulfur as active material, mixed with C65 and LA133 in the same mass ratio of 60:30:10. The slurry

was similarly prepared in H_2O/ethanol (V:V = 1:1) solution and coated, subsequently dried under identical conditions. The sulfur loading was matched to that of SPAN-based electrodes to enable direct comparison.

2.3 | Fabrication of Carbon-Modified Separator (C65 separator)

The carbon-modified separator was fabricated using the Doctor Blade technique. A slurry consisting of carbon 65 and LA133 with a mass ratio of 7:3 was prepared in H_2O/ethanol solution (V:V = 1:1) at room temperature; the solvent/solid material ratio was 10:1 (in mass ratio). The resulting slurry was stirred with a magnetic stirrer for 24 h at room temperature. Then, this slurry was blade-coated onto one side of the separator with a wet thickness of 150 µm (Whatman, Glass fiber-D). The solvent was removed by drying the coated separator at 60°C under vacuum for 12 h. Subsequently, discs with a diameter of 12 mm were punched out for cell assembly. The mass loading of the C65 coating layer (containing binder) on the separator is about 1.77 mg ± 0.1 cm^{-2}, and the C65 in the coating layer loading is 1.24 mg ± 0.1 cm^{-2}.

2.4 | Electrochemical Cells Assembly

The three-electrode Swagelok cell was assembled in an argon-filled glove box (O_2< 0.5 ppm, H_2O<0.5 ppm). The sulfur-containing polymer cathode was used as the working electrode, while sodium discs (10 mm diameter discs) served as the counter and reference electrodes. The electrolyte was composed of 1.0 M $NaCF_3SO_3$ (Tokyo Chemical Industry, >98.0%) dissolved in TEGDME (Thermo Fisher, 99%), with a fixed volume of 75 µL per cell.

2.5 | Materials Characterization

2.5.1 | X-Ray Diffraction

The XRD patterns of SPAN were collected and recorded on a STOE STADI P COMBI diffractometer with Mo-Kα1-radiation (λ = 0.7093 Å with focusing Ge 111 monochromator) in Debye-Scherrer geometry at room temperature. The Rietveld analysis of the XRD pattern was performed using the FullProf Suit package, including WinPLOTR, and the diffractogram was collected from 2 to 50°

2.5.2 | Elemental Analysis

Elemental analysis was performed with an Elementar Vario EL device (Elementar, Germany), under an Argon atmosphere, and three parallel tests were conducted on each sample for reproducibility.

2.5.3 | In Situ Raman Spectroscopy

In situ Raman spectroscopy was used to analyze the SPAN cathode. Raman spectroscopy was performed in situ with a 532 nm focused laser beam and a 10x objective lens (LadRAM HR Evolution, HORIBAJobin Yvon). This experiment used an in situ cell with a sapphire window on the anode side, the sodium negative electrode, glass fiber separator, and SPAN positive electrode were punched to create a small hole in the center for the excitation beam. Data were collected at 15 min intervals during the charge–discharge process. Baseline calibration was taken for all data.

2.6 | Electrochemical Characterization

The electrochemical experiments were conducted using a VMP-3 potentiostat (BioLogic Science Instruments). Galvanostatic charge and discharge were performed in different voltage windows between 0.5 and 2.7 V (vs Na^+/Na), 1.2–2.7 V (vs Na^+/Na), and 1.4–2.7 V (vs Na^+/Na). Cyclic voltammetry (CV) was performed at 1.2–2.7, 1.4–2.7, 1.6–2.7, 1.8–2.7 V under scanning rate of 0.1, 0.2, 0.5, and 0.8 mV s^{-1}. All cells were tested in a climate chamber at 25°C. The rate performance was evaluated at specific currents of 500, 1000, 2000 between 1.2 and 2.7 V. The long-term cycling was tested at a constant current of 500 mA g^{-1} for 200 cycles between 1.2 and 2.7 V. All capacity is calculated by mass of sulfur in cathode, for SPAN it is calculated by sulfur content of SPAN.

3 | Result and Discussion

3.1 | Synthesis and Characterization of Materials

To validate the synthesis, elemental analysis was used to determine the sulfur content, which was found to be 44.3% (Table S1). Additionally, an X-ray diffractometer (XRD) was employed to confirm the structural characteristics of SPAN [19]. The XRD pattern reveals that SPAN is amorphous without any diffraction peaks from crystalline domains of S_8, indicating that elemental sulfur had successfully bonded with PAN to form a sulfur-containing polymer network [20] (Figure S1).

3.2 | Electrochemical Behavior of SPAN

CV is used to study the electrochemical behavior of SPAN between 0.5 and 2.7 V (vs Na^+/Na). As shown in Figure 1a, during the initial reduction process, SPAN exhibits a reduction peak centered at 1.2–1.5 V. This peak is generally associated with the sodiation of short sulfur chains covalently bonded within the SPAN framework, leading to the formation of short-chain polysulfides and Na_2S [21]. Owing to the absence of free S_8 or long sulfur chains in pristine SPAN, no distinct reduction features related to long-chain polysulfides are observed in the initial discharge process [22]. In the subsequent anodic scan, a pronounced oxidation peak appears at around 1.7–1.9 V, which can be attributed to the partial desodiation of Na_2S and the regeneration of sulfur species confined within the SPAN structure [23]. In addition, a weak and broad oxidation feature located between 2.2 and 2.5 V is observed in the first cycle. This feature has been reported in previous studies and is commonly associated with the oxidation of higher-order polysulfide species [24]. However, its low intensity suggests that only a limited amount

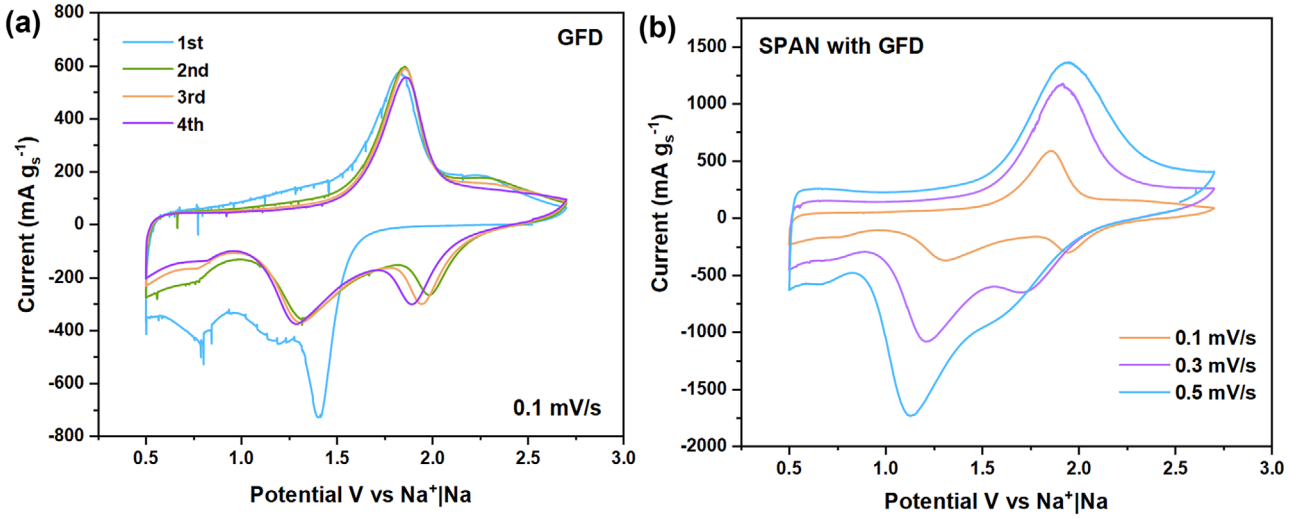

FIGURE 1 | (a) CV curve of SPAN electrode at 0.1 mV s^{-1}, (b) CV curve of SPAN electrode at different scan rates.

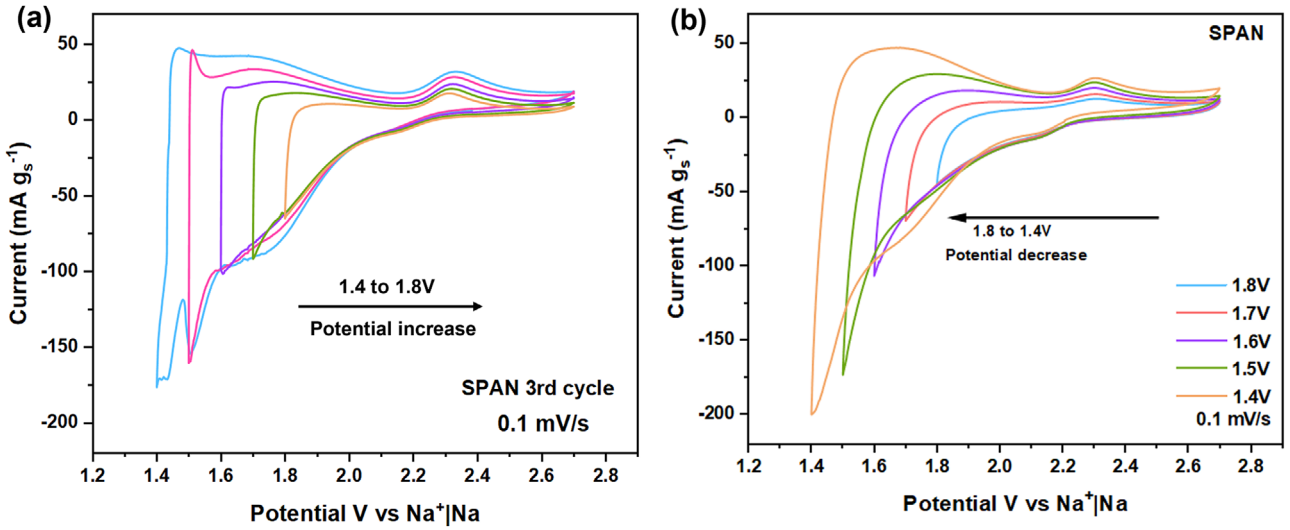

FIGURE 2 | (a) CV curve test with potential opening with the lowest cut-off from low to high, (b) CV curve test with potential opening with the lowest cut-off from high to low.

of such species may be involved [25]. After the first cycle, a new cathodic peak appears at around 2.0 V. The appearance of this peak indicates a change in the reduction behavior after the initial electrochemical activation. This phenomenon can be attributed to the incomplete reincorporation of sulfur species formed during the first cycle into the SPAN backbone, giving rise to weakly confined or electrolyte-accessible polysulfides that participate in subsequent redox processes [26]. Notably, after three cycles, the broad and small oxidation peak in the 2.2–2.5 V range disappears and does not reappear in subsequent cycles with higher scan rates (as shown in Figure 1b).

To clarify the reasons for the disappearance of the small and broad peak between 2.2 and 2.5 V, CV curves (Figure 2a) were recorded within varying potential ranges (i.e., 1.4–2.7, 1.5–2.7, 1.6–2.7, 1.7–2.7, and 1.8–2.7 V). It is worth noting that after repeated cycles within a small range, the small peak between 2.2 and 2.5 V remains unchanged. This result indicates that the reduction reactions occurring below 1.4 V cause the disappearance of the small high-voltage oxidation peak. To further support this conclusion, narrow range CV tests were conducted from the direction high to low potential using the same SPAN//Na cell to avoid the impact of possible irreversible reactions on further cycles that may exist at lower potentials (Figure 2b).

Figure 2b shows that by pushing the potential progressively to lower values (i.e., by pushing the reduction reaction), the broad oxidation peak between 2.2 and 2.4 V increases, indicating that this oxidation process is a response to the reduction reaction. However, when the voltage drops down to 1.0 V (as shown in Figure 3), the small peak between 2.2 and 2.4 V becomes broader and hidden by the capacitive current. However, when the lower cut-off voltage increases from 1.0 to 1.2 V, the small oxidation peak between 2.2 and 2.4 V can be clearly observed again and becomes

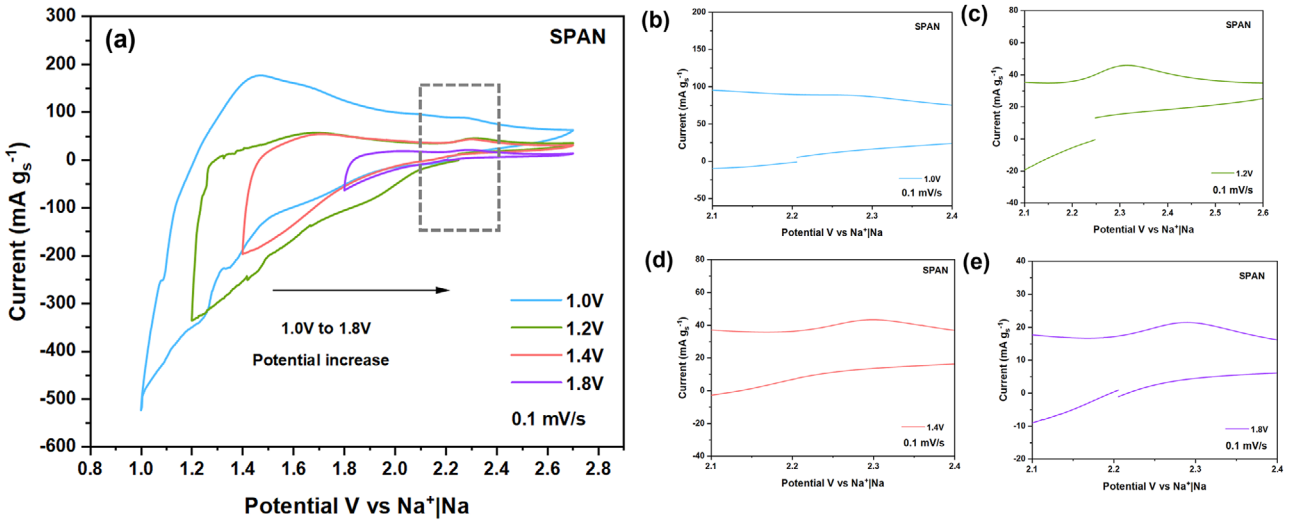

FIGURE 3 | (a) CV curve of SPAN battery scanned with different lower potential cut-off (from low to high), (b–e) Enlarged view of the CV curves between 2.1–2.4 V.

more pronounced when the lower cut-off voltage rises to 1.8 V. This result indicates that the deep discharge in the low-voltage region eventually inhibits the oxidation reaction between 2.2 and 2.4 V.

In order to further observe the reaction during the deep discharge process of the SPAN cell, in-situ Raman spectroscopy was conducted during the complete discharge–charge process of the SPAN cell from 0.5 to 2.7 V. As shown in Figure 4a, the peaks observed at 313, 370, 394, and 805 cm^{-1} in the SPAN spectrum correspond to the vibrations of C–S bonds, confirming the presence of covalent carbon–sulfur linkages within the polymer structure. Furthermore, additional peaks detected at 473 and 936 cm^{-1} are attributed to the ring-stretching modes of S–S bonds. Finally, the most intense signals at 1345 and 1550 cm^{-1} were assigned to the D and G bands typical of carbonaceous materials [25]. After cell assembly, the SPAN electrode exhibits a modified spectrum due to slight sulfur dissolution. A decrease in the intensity of the C–S bond signals is observed, along with the emergence of characteristic dissolution products, including long-chain polysulfide ions (S_x) at 483 cm^{-1} and S_3^- species at 534 cm^{-1}. It is worth noting that a distinct signal is present at 534 cm^{-1} from the very beginning. This feature may arise from the stacking background associated with S–S bonds, which typically appear in the 430–550 cm^1 [27]. The D and G bands disappear after the electrode comes into contact with the electrolyte because a passivating cathode electrolyte interphase (CEI) forms. After sodiation to 0.57 V, the D band becomes visible again. This reappearance occurs because sodium ions begin to interact with and insert into the carbonaceous SPAN framework once the CEI has already formed, and this insertion induces increased structural changes that restore the Raman activity associated with the D band. At the beginning of discharge, the Raman spectrum exhibits a Raman peak located at 460 cm^{-1}, which usually corresponds to short-chain sulfur in SPAN. During the discharge to 0.5 V, this signal gradually weakens, corresponding to the breakage and reduction of short-chain sulfur in SPAN. When the potential is below 1.0 V, a significant increase in Raman signals was observed at 423 cm^{-1} (C–S), 534 cm^{-1} (S_3^- species), and 1345 cm^{-1} (D band) (Figure 4b,c) [28]. The above results indicate that during low-voltage discharge (below 1.0 V), sodium ions form irreversible interactions with the C or N atoms within the SPAN. This process increased structural disorder within the carbonaceous framework, which contributes to the enhancement of the D-band signal [29, 30]. Meanwhile, the enhanced C–S vibrational signal from the presence of short-chain sulfur fragments transiently adsorbed at defect-rich carbon sites. This demonstrates that deep discharge can accumulate free S_3^- ions in the electrolyte, resulting in the reconstruction of the SPAN structure.

During the charge process at around 2.0 V, the Raman signal in the range of 400–500 cm^{-1} remained at high intensity, which corresponds to polysulfides (Na_2S_x, $2<x<6$) [28]. This indicates that the polysulfides do not reversibly oxidize back, and they are accumulating as soluble species consistently (Figure 4b,c).

The soluble species can react with sodium at the subsequent discharge and show a new reduction peak around 2.0 V in CV (Figure 1a). At the same time, compared to the initial discharge state, the Raman peak intensity at 460 cm^{-1} (corresponding to sulfur–sulfur chain in SPAN) decreased significantly at the cut-off charge voltage (2.7 V) (Figure 4d). This result can further indicate that the sulfur–sulfur chain in SPAN cathode is unable to comprehensively reform in the charge process after deep discharge, which is due to the sulfur loss caused by accumulation and shuttle effect of S_3 ions in electrolyte. This behavior directly explains the evolution of the 2.2–2.4 V oxidation peak in CV (Figure 3). This peak corresponds mainly to the oxidation of surface-anchored intermediate-valence sulfur species, rather than soluble S_3^-. Under shallow discharge (higher than 1.0 V), sulfur is partially reduced and confined near the SPAN surface. Therefore, these species can be re-oxidized during charging, showing a distinct peak at 2.2–2.4 V. In contrast, most sulfur is converted into highly soluble S_3^- species under deep discharge (lower than 1.0 V), which dissolve into the ether electrolyte and undergo polysulfide shuttling. With continued cycling, the amount of polysulfides that remain at the cathode surface and are

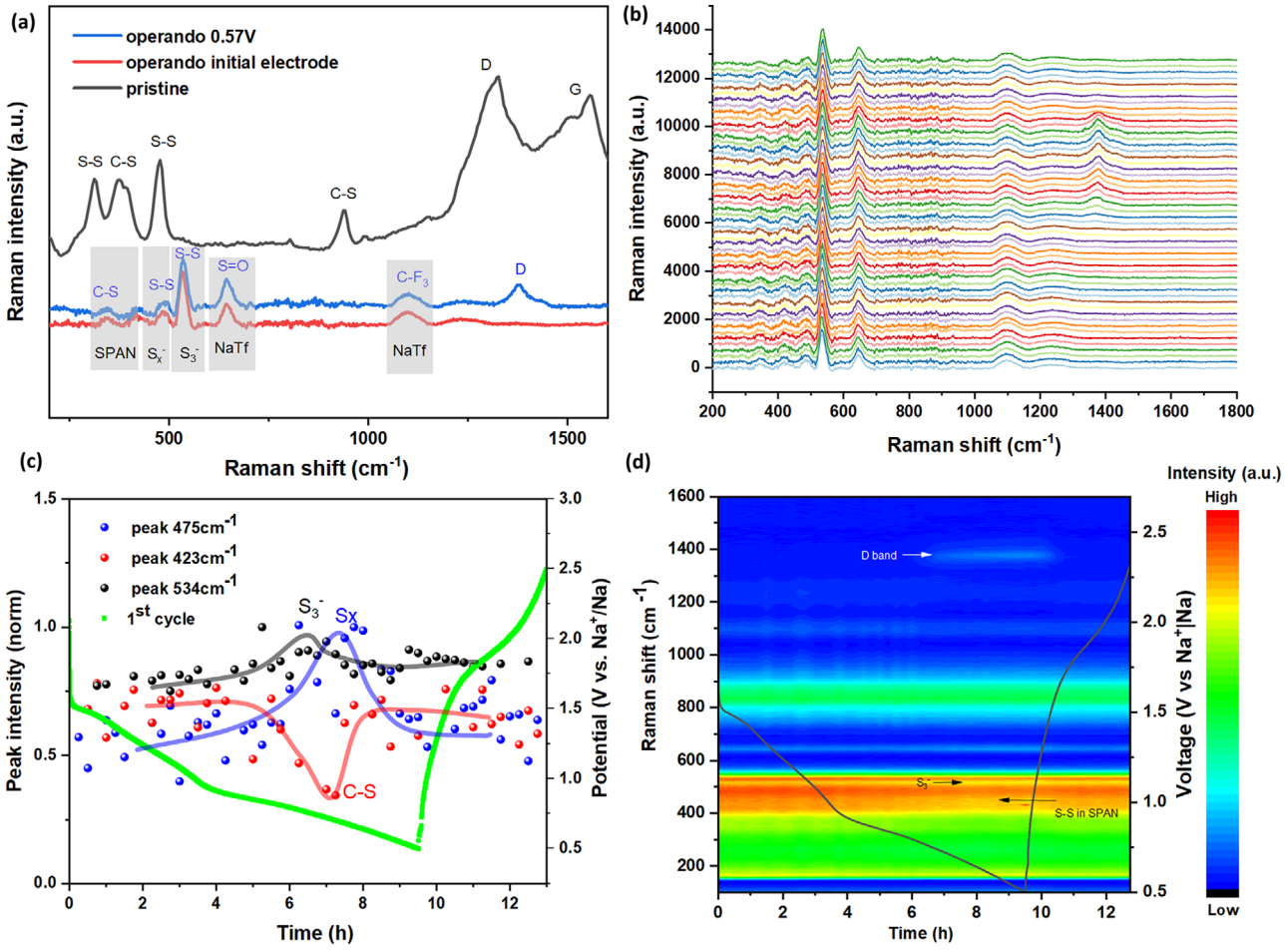

FIGURE 4 | (a) Ex situ Raman spectra of SPAN and in situ Raman spectra of fresh SPAN cell/discharge at 0.57 V. (b) Linear diagram of in situ Raman spectra of SPAN cell during discharge–charge process between 0.5 and 2.7 V. (c) Raman peak intensity of C–S, S_3^- and S_x during charge–discharge between 0.5 and 2.7 V. (d) In situ Raman spectra of SPAN cell during discharge–charge process between 0.5 and 2.7 V.

electrochemically accessible for oxidation at 2.2–2.4 V gradually decreases and eventually becomes negligible. As a result, the 2.2–2.4 V peak progressively disappears with increasing discharge depth. Galvanostatic charge and discharge cycles were performed between 0.5 and 2.7 V at 500 mA g^{-1}, and the curves are shown in Figure 5a. After a few cycles between 0.5 and 2.7 V, the SPAN electrode exhibits an abnormal plateau at approximately 2.0–2.2 V, unable to continue rising, which indicates a possible internal micro-short circuit due to local dendrite formations. This could be due to the polysulfides formed at such a low potential (proved by Raman test in Figure 4), which could shuttle to the sodium anode where they react [31]. This may consequently cause a large amount of sodium sulfide to cover and block the sodium surface, and therefore make the sodium anode locally inactive. In this situation, the current cannot be evenly distributed on the surface of the sodium electrode, and it will accumulate only at sites where sodium is not covered by sodium sulfide. This also means that the current is locally higher, and that the probability of dendrite growth at these sites is much higher. The uneven distribution of current leads to easier dendrite growth, which can cause the occurrence of micro short circuits and therefore the impossibility to charge [32].

On this basis, the charging step was stopped and the current reversed. After discharge, the electrode can undergo further cycling, pointing towards the partial dissolution of the Na dendrites. However, with repeated deep charge discharge processes, the shuttle effect and the regeneration of soft sodium dendrites may occur again, resulting in the observed abnormal charging curves at around 2.0 V (Figure 5b).

In order to avoid effects due to the deep discharge, a fresh SPAN electrode was cycled between 1.4 and 2.7 V, and the results are shown in Figure S3a. In the first discharge, the SPAN electrode delivers 315mAh g^{-1} at a specific current of 500 mA g^{-1}, but it only exhibits a capacity of about 50 mAh g^{-1} during the first charge, a value that remains stable in subsequent cycles. This result indicates that when the lower potential cut-off is limited to 1.4 V, a part of the reaction is strongly irreversible, which makes capacity decay between the first and second cycle, and the conversion of short-chain polysulfides to sodium sulfide is incomplete, which obviously leads to a drastic decrease in capacity [33]. This result indicates that even if the reduction of the potential window may improve the electrode stability, this has the drawback of very low capacity.

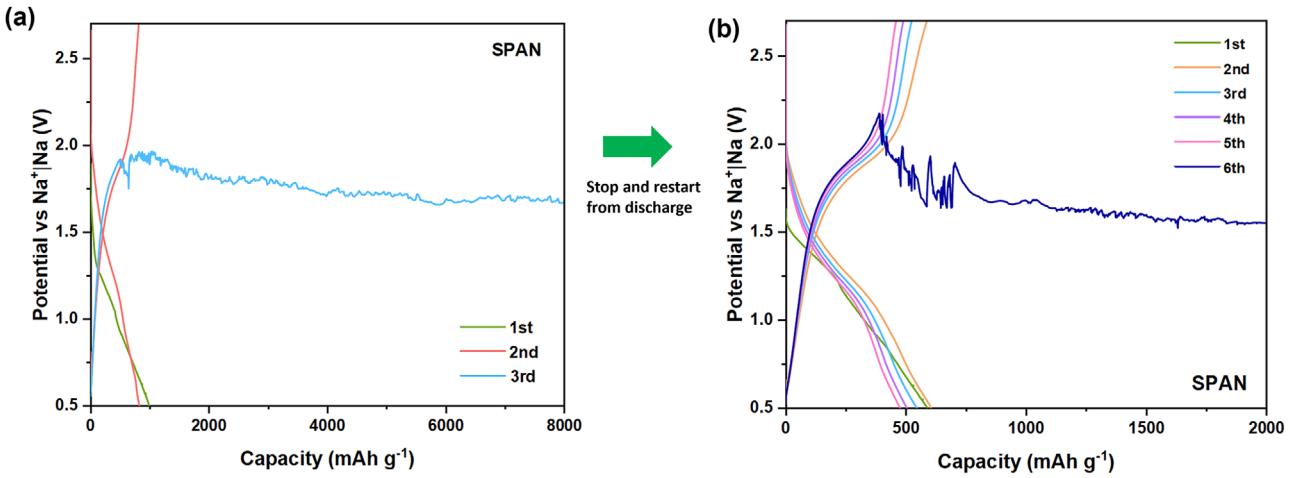

FIGURE 5 | (a) Charge–discharge curve of SPAN battery between 0.5 and 2.7 V. (b) Charge–discharge curve of SPAN battery between 0.5 and 2.7 V after abnormal charge. (Electrolyte: 1.0 M $NaCF_3SO_3$ in TEGDME, capacity is calculated by sulfur content of cathode, sulfur loading = 0.8 mg cm^{-2}).

In another experiment, the SPAN cell in Figure 5, which was first pre-cycled between 0.5 and 2.7 V at 500 mA g^{-1} for 9 cycles (and showed an abnormal charge curve due to the soft dendrites), was further cycled in the restricted voltage range between 1.4 and 2.7 V at 500 mA g^{-1} (Figure S3). This pre-cycled cell now shows stable and reversible charge–discharge curves in the range 1.4–2.7 V at various current densities. This further supports the conclusion that the dissolution of sodium micro dendrites during the discharge process can alleviate microshort circuits; moreover, avoiding a deep discharge can effectively prevent the formation of irreversible polysulfide products and the occurrence of sodium dendrites. Furthermore, this pre-cycled cell delivers higher capacity than the cell cycled directly between 1.4 and 2.7 V. This could be ascribed to the fact that polysulfide accumulated in the electrolyte at low potential can participate in subsequent reactions, providing capacity. This is consistent with the conclusion that polysulfides accumulated during deep discharge can be partially reversed during the charging process. It is worth noting that the cells pre-cycled between 0.5 and 2.7 V have coulombic efficiency (CE) closer to 100% during the first 10 cycles between 1.4 and 2.7 V, while the cell without pre-cycling has CE about 110%. This can be due to the irreversible reactions that have already occurred during pre-cycling. This kind of "pre-irreversible reactions" may be associated with the irreversible interaction between sodium ions and the SPAN [34], which can help the cell to reach a reversible reaction during subsequent cycles. It can be observed from the CE of the 10^{th} cycle to the 20^{th} cycle and from the 30^{th} cycle to the 40^{th} cycle. Between the range of 10^{th} cycle to 20^{th} cycle, the cell without pre-cycling has CE of about 102%, and between the range of 30th cycle to 40th cycle, the cell without pre-cycling has CE about 107%. This result can indicate irreversible reaction in each cycle, while the cell with pre-cycling has CE of about 100% in the above two ranges (Figure S3e) [35].

3.2.1 | Electrochemical Performance Comparison at a Reasonable Cut-Off Voltage

Considering the previous experiments, where we observed that deep discharge to 0.5 V may be detrimental, and a too shallow discharge down to 1.4 V does not provide enough capacity, in the following experiments, we decided to cycle the cell between 1.2 and 2.7 V and compared the SPAN electrode with elemental sulfur cathode (sulfur loading = 1 mg cm^{-2}, carbon content = 30%, prepare by slurry coating). The cells have been cycled at currents between 500 and 2000 mAh g^{-1}. Clearly, the SPAN electrode delivers higher capacity at all currents (Figure 6a) and longer stability (Figure 6b) than the sulfur cathode, probably due to the conjugated structures in SPAN and the short sulfur chain. The initial capacity of the SPAN electrode is 550mAh g^{-1} at the first cycle at 500 mA g^{-1}, and it decays to 250 mAh g^{-1} at the second cycle. After 100 cycles, 200 mAh g^{-1} of capacity is retained. The comparison of the coulombic efficiency (Figure S4) further proves that SPAN can provide a more reversible sulfur conversion reaction by reasonable selection of the potential window, and the short-chain sulfur in SPAN can prevent the generation of long-chain polysulfides.

The SPAN//Na cell has a coulombic efficiency of around 99.86% during the first 20 cycles and stays at 100% during the last 80 cycles at 500 mA g^{-1}. In contrast, the coulombic efficiency of the sulfur cathode is only 60-80%. This is because the shuttle effect caused by the polysulfides inside the cell causes continuous loss of sulfur [36]. At the same time, electron transfer on the cathode side may be hindered by the insulating properties of sulfur, which has a carbon content of 30% (similar to SPAN cathodes), resulting in high polarization and low reversibility of the cell [37]. Compared with sulfur, the SPAN cathode has high conductivity of 10^{-4} S cm^{-1}, which is much higher than the conductivity of the sulfur cathode, which is 10^{-30} S cm^{-1} [38, 39]. Such high conductivity can [40] reduce the polarization of the cell and improve the reversibility of the reaction between sulfur and sodium [41].

Figure S5 shows the charge–discharge curve of SPAN and sulfur. During the discharge process, the sulfur cathode exhibits a typical dual-platform feature, with the two platforms corresponding to the $Na_2S_8 \rightarrow Na_2S_6/Na_2S_4$ conversion process and the $Na_2S_4 \rightarrow Na_2S_2/Na_2S$ conversion process, respectively [42]. In contrast, the SPAN cathode only exhibits a sloped curve, which indicates a one-step reaction without phase transitions rather than the $Na_2S_8 \rightarrow Na_2S_6/Na_2S_4$ conversion process: the

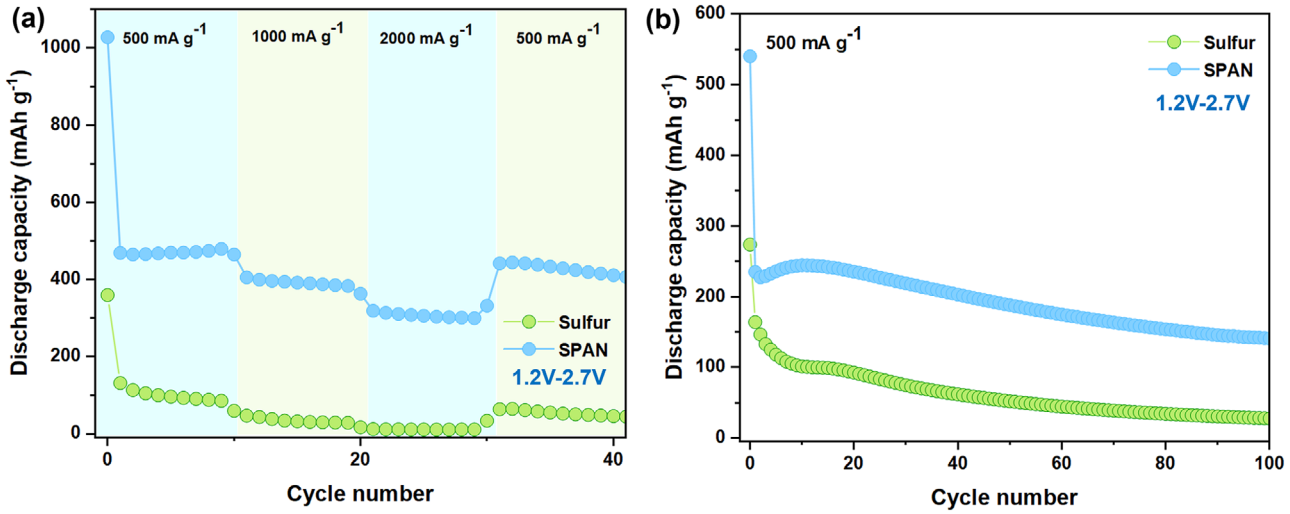

FIGURE 6 | (a) Rate performance of battery cell with SPAN and sulfur cathode, (b) long cycling performance at 500 mA g^{-1} of battery cell with SPAN and sulfur cathode. (Electrolyte: 1.0 M $NaCF_3SO_3$ in TEGDME, capacity is calculated by sulfur content of cathode, sulfur loading = 0.8 mg cm^{-2}).

short-chain polysulfides are directly converted into sodium sulfide through a solid-state transformation [43]. During the charging process, the sulfur cathode exhibits a charging capacity that far exceeds the discharge capacity, which is attributed to the overcharge effect caused by polysulfides [44]. At the same time, the high potential difference between the charge and the discharge curves indicates the high cell polarization [45]. In contrast, the SPAN cathode exhibits a charging capacity that is almost identical to the discharge capacity, indicating an orderly and highly reversible sulfur–sodium conversion reaction, and significantly lower polarization [46]. However, one drawback is that the average voltage of the SPAN//Na cell is generally lower than that of sulfur//Na cell, which leads to lower energy density.

Figure S6 shows the Raman spectra of a fresh SPAN electrode compared t a SPAN electrode after two cycles and four cycles between 1.2 and 2.7 V. Two Raman peaks can be observed at 312 and 372 cm^{-1}, which belong to the C–S bond in SPAN [47, 48]. Meanwhile, the Raman peak observed at 477 cm^{-1} belongs to the S–S bond in SPAN [49]. After two complete charge–discharge cycles (ending at 2.7 V), the Raman signal intensity of C–S and S–S bonds decreased, indicating that the reformation of C–S and S–S bonds is not completely reversible in the first cycle [50]. Then, the cell cycled for two cycles was compared with the cell after four complete charge–discharge cycles, and the signal strength of the C–S bond and the S–S bond remained the same. This indicates that under shallow discharge conditions (1.2 V), the absence of significant S_3^- accumulation prevents sulfur loss through polysulfide shuttling. As a result, the C–S and S–S signals remain well preserved after cycling. Further investigation on the structural evolution of SPAN between 1.2 and 2.7 V is provided by in situ Raman spectroscopy. As shown in Figure 7c, the D-band signal near 1350 cm^{-1} did not exhibit noticeable enhancement during the charge–discharge process, suggesting that the carbon backbone of SPAN remained structurally stable. Moreover, enhancement of the signal associated with S_3^- species was not observed at the end of discharge (1.2 V), which is different compared to the behavior during deep discharge to 0.5 V (Figure 7b).

To further optimize the SPAN//Na cell, a carbon-modified functional separator (as a polysulfide blocking layer) was implemented and discussed in the next section.

3.2.2 | Application of a Functional Separator to Improve Capacity Retention

Carbon functional separator with a high specific surface area and porous structure can inhibit shuttle effects by physically adsorbing soluble polysulfides [51, 52]. Moreover, it can provide an electron transport path for the positive electrode, thereby accelerating the conversion reaction kinetics and enhancing the utilization rate of active materials [53]. For this research, C65 was used as a functional carbon layer for the separator, which has a high surface area (62 m^2 g^{-1}) and high conductivity [54]. To exclude the contribution to the capacity by the carbon layer (C65:LA133 = 7:3 in mass ratio) applied to the separator, electrochemical tests were performed by sandwiching the separator between an Al current collector and the Na counter electrode. The carbon layer of the separator is directly contacting the Al current collector. As shown in Figure S2, it can be seen that the C65 | Na cell delivers only 0.045 mAh g^{-1} capacity at 500 mA g^{-1} and rapidly decays to 0.03 mAh g^{-1} during charging, indicating that no additional capacity is contributed by the material coated on the functional separator.

Figure 8a shows the charge and discharge curves of SPAN with the CGFD separator and the GFD separator at 500 mA g^{-1}. The cell with the CGFD separator shows higher capacity. The SPAN with the CGFD separator delivers reversible capacity 1202 mAh g^{-1} in the first cycle at 500 mA g^{-1}, which indicates that the CGFD separators can significantly inhibit the shuttle effect in the cell to improve the capacity [55–57].

Figure 8b shows the significantly improved rate performance of the cell containing the CGFD separator. The cell with the CGFD-based cell exhibits specific capacities of 1787, 598, and 318 mAh g^{-1} at 500, 1000, and 2000 mAh g^{-1}. At the same time, it also shows

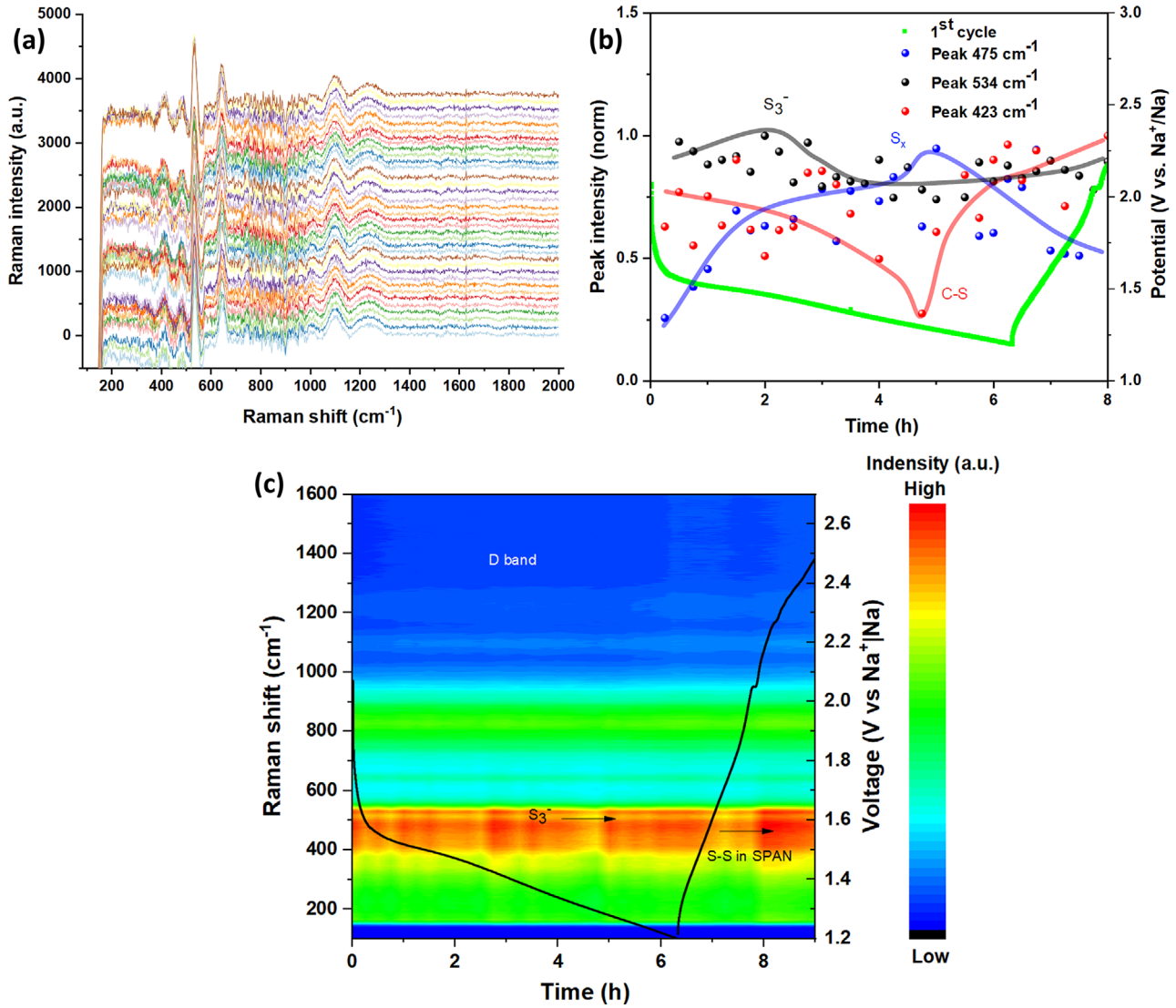

FIGURE 7 | (a) Linear diagram of in situ Raman spectra of SPAN cell during discharge–charge process between 1.2 to 2.7 V. (b) Raman peak intensity of C–S, S_3^- and S_x during charge–discharge between 1.2 and 2.7 V. (c) In situ Raman spectra of SPAN cell during discharge–charge process between 1.2 to 2.7 V.

474 mAh g^{-1} after cycling under different rates, which reflects the help of the CGFD separator in impeding the shuttling.

The two cells were compared in terms of long cycling stability at 500 mA g^{-1}. The cell with the CGFD separator shows a high capacity of 2186 mAh g^{-1} in the first cycle, and can get a higher capacity than the battery with the GFD separator after 100 cycles. Nevertheless, the capacity of the modified separator decays faster than that of the cell with GFD. Apparently, the CGFD separator can help in the initial cycles, but is not suitable for stabilizing the electrochemical reaction between SPAN and sodium. The same conclusion can be proved by CE. Figure 6d shows the coulombic efficiency (CE) of cells with the CGFD separator and the GFD separator. Compared to the GFD cell, the CGFD cell exhibits a CE of 98.92% at the first cycle, and then increases to 100% after 5 cycles. At the 32nd cycle, the CE suddenly decreased to 72.42%, and back to 100% at the 33rd cycle. The same sudden decrease can be observed at the 44th and 48th cycles. This can indicate that the side reaction happened in the cell with CGFD, and the application of carbon functional separators still needs to be optimized.

4 | Conclusion

This study demonstrated the electrochemical performance of sulfurized polyacrylonitrile (SPAN) as a positive electrode material for room-temperature sodium–sulfu (RT Na-S) batteries with ether-based electrolytes under high current density. In ether-based electrolytes, deep discharge (e.g., down to 0.5 V) can lead to accumulation of S_3^-. It causes accumulation of soluble polysulfides in the electrolyte. This accumulation exacerbates the shuttle effect and the generation of inactive sites on the sodium negative electrode, which leads to uneven current distribution at the negative electrode interface. Uneven current distribution can facilitate the development of sodium dendrites, leading to the formation of micro-short circuits in the battery. This conclusion indicates the necessity of avoiding deep discharge in ether-based

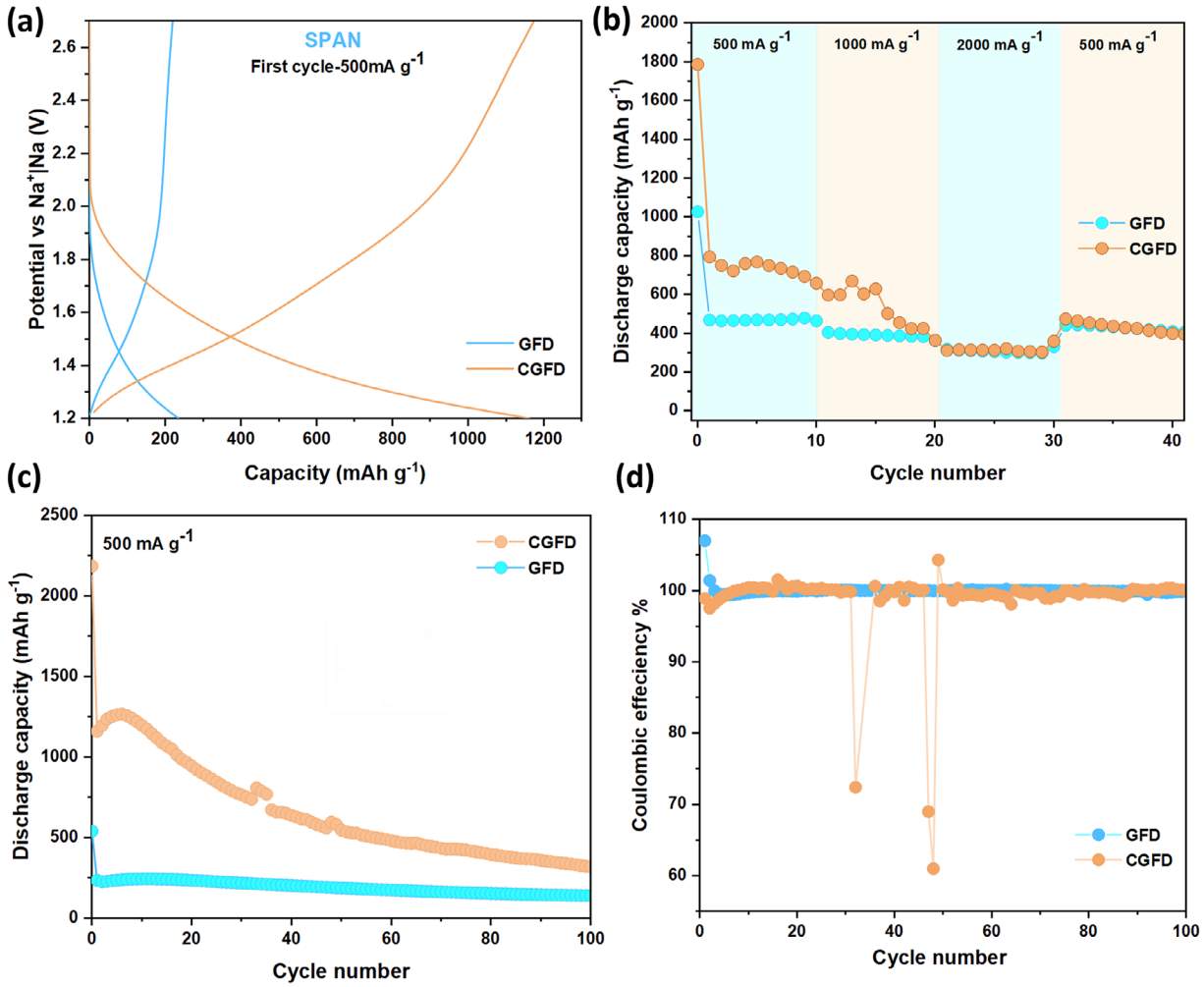

FIGURE 8 | (a) Charge–discharge curve of SPAN//Na cell with CGFD and GFD, b) rate performance of SPAN//Na cell with CGFD and GFD separators, (c) long cycle performance of SPAN//Na cell with CGFD and GFD. (d) Coulombic efficiency of SPAN//Na cell with CGFD and GFD. (Electrolyte: 1.0 M $NaCF_3SO_3$ in TEGDME, capacity is calculated by sulfur content of cathode, sulfur loading = 0.8–1 mg cm^{-2}).

SPAN-sodium batteries. However, it should be noted that a much higher cut-off voltage is also not necessarily better, and a reasonable cut-off voltage should be chosen. Excessively high cut-off voltage (such as 1.4 V) can lead to incomplete sulfur–sodium reaction, resulting in a significantly lower capacity. According to our findings, the most suitable discharge cut-off voltage is 1.2 V, which can avoid micro short circuits and the generation of a large amount of soluble polysulfides. As a further improvement, a carbon functional separator can help SPAN electrodes to achieve higher capacity due to confinement of the reduced species to the cathode side of the cell. However, although a positive effect of the functional separator has been observed, further optimization is required to achieve better stability.

Acknowledgements

This work contributes to the research performed at CELEST (Center for Electrochemical Energy Storage Ulm-Karlsruhe), and was funded by the German Research Foundation (DFG) under Project ID 390874152 (POLiS Cluster of Excellence, EXC 2154) and by the Eucor Seed Money Project "FuseTheWaste." As a Ph.D. student at IAM-ESS in Karlsruhe Institute of Technology, Liwen Yang received financial support from China Scholarship Council (CSC) under File No. 202206240016. We greatly appreciate Nicole Klaassen for her support in Elemental analysis. The authors are also thankful to Guizhou Provincial Youth Guiding Fund Project (Grant No. [2025]065), and Rui Chen and Yuanyuan Chen for them support in In-Situ Raman test. H.M. acknowledges UHA for the financial support from the French National Research Agency with the reference "ANR-22-CPJ1-0077-01" (particularly for covering the first two years of the PhD studies of B.P.), the Department of Chemistry, RPTU University Kaiserslautern-Landau and the support from the Ministry of Science of Rhineland-Palatinate.

Open access funding enabled and organized by Projekt DEAL.

Conflicts of Interest

The authors declare no conflicts of interest.

Data Availability Statement

The data that support the findings of this study are openly available in Zenodo at https://doi.org/10.5281/zenodo.17935478, reference number 17935478.

References

1. G. G. Njema, R. B. O. Ouma, and J. K. Kibet, "A Review on the Recent Advances in Battery Development and Energy Storage Technologies,"

Journal of Renewable Energy 2024, no. 1 (2024): 2329261, https://doi.org/10.1155/2024/2329261.

2. J. Lin, X. Zhang, E. Fan, R. Chen, F. Wu, and L. Li, "Carbon Neutrality Strategies for Sustainable Batteries: From Structure, Recycling, and Properties to Applications," *Energy & Environmental Science* 16, no. 3 (2023): 745–791, https://doi.org/10.1039/D2EE03257K.

3. B. Wang, W. A. Abdulla, D. Wang, and X. S. Zhao, "A Three-Dimensional Porous $LiFePO_4$ Cathode Material Modified with a Nitrogen-Doped Graphene Aerogel for High-Power Lithium Ion Batteries," *Energy & Environmental Science* 8, no. 3 (2015): 869–875, https://doi.org/10.1039/C4EE03825H.

4. S. Nyamathulla and C. Dhanamjayulu, "A Review of Battery Energy Storage Systems and Advanced Battery Management System for Different Applications: Challenges and Recommendations," *Journal of Energy Storage* 86 (2024): 111179, https://doi.org/10.1016/j.est.2024.111179.

5. L. Zhao, Y. Tao, Y. Zhang, et al., "A Critical Review on Room-Temperature Sodium-Sulfur Batteries: From Research Advances to Practical Perspectives," *Advanced Materials* 36, no. 25 (2024): 2402337, https://doi.org/10.1002/adma.202402337.

6. Z. W. Seh, J. Sun, Y. Sun, and Y. Cui, "A Highly Reversible Room-Temperature Sodium Metal Anode," *ACS Central Science* 1, (2015): 449–455, https://pubs.acs.org/doi/full/10.1021/acscentsci.5b00328.

7. M. S. Syali, D. Kumar, K. Mishra, and D. K. Kanchan, "Recent Advances in Electrolytes for Room-Temperature Sodium-Sulfur Batteries: A Review," *Energy Storage Materials* 31 (2020): 352–372, https://doi.org/10.1016/j.ensm.2020.06.023.

8. Y. Qi and M. Xu, "Engineering towards Stable Sodium Metal Anodes in Room Temperature Sodium-Sulfur Batteries: Challenges, Progress and Perspectives," *Energy Storage Materials* 72 (2024): 103704, https://doi.org/10.1016/j.ensm.2024.103704.

9. Y. Wang, J. Chai, Y. Li, et al., "Strategies to Mitigate the Shuttle Effect in Room Temperature Sodium–Sulfur Batteries: Improving Cathode Materials," *Dalton Transactions* 52, no. 9 (2023): 2548–2560, https://doi.org/10.1039/D3DT00008G.

10. H. W. Liu, W. H. Lai, Y. J. Lei, et al., "Electrolytes/Interphases: Enabling Distinguishable Sulfur Redox Processes in Room-Temperature Sodium-Sulfur Batteries," *Advanced Energy Material* 12 (2022): 2103304, https://onlinelibrary.wiley.com/doi/full/10.1002/aenm.202103304.

11. L. Lin, C. Zhang, Y. Huang, et al., "Challenge and Strategies in Room Temperature Sodium–Sulfur Batteries: A Comparison with Lithium–Sulfur Batteries," *Small* 18, no. 43 (2022): 2107368, https://doi.org/10.1002/smll.202107368.

12. S. Wei, H. Zhang, Y. Huang, W. Wang, Y. Xia, and Z. Yu, "Pig Bone Derived Hierarchical Porous Carbon and Its Enhanced Cycling Performance of LithiumSulfur Batteries," *Energy & Environmental Science* 4, no. 3 (2011): 736–740, https://doi.org/10.1039/C0EE00505C.

13. G. Zheng, Y. Yang, J. J. Cha, S. S. Hong, and Y. Cui, "Hollow Carbon Nanofiber-Encapsulated Sulfur Cathodes for High Specific Capacity Rechargeable Lithium Batteries," *Nano Letters* 11, no. 10 (2011): 4462–4467, https://doi.org/10.1021/nl2027684.

14. X. Yao, J. Xu, Z. Hong, et al., "Metal/Graphene Composites with Strong Metal–S Bondings for Sulfur Immobilization in Li–S Batteries," *The Journal of Physical Chemistry C* 122, no. 6 (2018): 3263–3272, https://doi.org/10.1021/acs.jpcc.7b12063.

15. T. Ma, H. Yue, Y. Xiao, et al., "A Review of Organic Sulfur Applications in Lithium-Sulfur Batteries," *Journal of Power Sources* 625 (2025): 235717, https://doi.org/10.1016/j.jpowsour.2024.235717.

16. X. Zhao, C. Wang, Z. Li, X. Hu, A. A. Razzaq, and Z. Deng, "Sulfurized Polyacrylonitrile for High-Performance Lithium Sulfur Batteries: Advances and Prospects," *Journal of Materials Chemistry A* 9, no. 35 (2021): 19282–19297, https://doi.org/10.1039/D1TA03300J.

17. S. V. Klostermann, J. Kappler, A. Waigum, M. R. Buchmeiser, A. Köhn, and J. Kästner, "The Reduction Behavior of Sulfurized Polyacrylonitrile (SPAN) in Lithium–Sulfur Batteries Using a Carbonate Electrolyte: A Computational Study," *Physical Chemistry Chemical Physics* 26, no. 13 (2024): 9998–10007, https://doi.org/10.1039/D3CP06248A.

18. H. Kim, M. K. Sadan, C. Kim, et al., "Enhanced Reversible Capacity of Sulfurized Polyacrylonitrile Cathode for Room-Temperature Na/S Batteries by Electrochemical Activation," *Chemical Engineering Journal* 426 (2021): 130787, https://doi.org/10.1016/j.cej.2021.130787.

19. X. Wang, Y. Qian, L. Wang, et al., "Sulfurized Polyacrylonitrile Cathodes with High Compatibility in both Ether and Carbonate Electrolytes for Ultrastable Lithium–Sulfur Batteries," *Advanced Functional Materials* 29, no. 39 (2019): 1902929, https://doi.org/10.1002/adfm.201902929.

20. D. Liu, Z. Li, X. Li, et al., "Stable Room-Temperature Sodium–Sulfur Batteries in Ether-Based Electrolytes Enabled by the Fluoroethylene Carbonate Additive," *ACS Applied Materials & Interfaces* 14, no. 5 (2022): 6658–6666, https://doi.org/10.1021/acsami.1c21059.

21. S. Murugan, S. V. Klostermann, P. Schützendübe, G. Richter, J. Kästner, and M. R. Buchmeiser, "Stable Cycling of Room-Temperature Sodium-Sulfur Batteries Based on an in Situ Crosslinked Gel Polymer Electrolyte," *Advanced Functional Materials* 32, no. 32 (2022): 2201191, https://doi.org/10.1002/adfm.202201191.

22. C. Hao, H. Lu, J. Liu, et al., "Construction of Ordered and Fast Lithium Ion Channels in Gel Electrolytes for Li-SPAN Batteries," *ACS Applied Materials & Interfaces*, 16 (2024): 60288, https://pubs.acs.org/doi/full/10.1021/acsami.4c13415.

23. S. Murugan, S. V. Klostermann, W. Frey, J. Kästner, and M. R. Buchmeiser, "A Sodium Bis(perfluoropinacol) Borate-Based Electrolyte for Stable, High-Performance Room Temperature Sodium-Sulfur Batteries Based on Sulfurized Poly(acrylonitrile)," *Electrochemistry Communications* 132 (2021): 107137, https://doi.org/10.1016/j.elecom.2021.107137.

24. F. Jin, R. Wang, Y. Liu, et al., "Conversion Mechanism of Sulfur in Room-Temperature Sodium-Sulfur Battery with Carbonate-Based Electrolyte," *Energy Storage Materials* 69 (2024): 103388, https://doi.org/10.1016/j.ensm.2024.103388.

25. J. M. Blázquez-Moreno, A. L. Páez Jerez, A. Y. Tesio, A. Benítez, and Á. Caballero, "Stable Long-Term Cycling of Room-Temperature Sodium-Sulfur Batteries Based on Non-Complex Sulfurised Polyacrylonitrile Cathodes," *Batteries & Supercaps* 8, no. 5 (2025): 202400640, https://doi.org/10.1002/batt.202400640.

26. X. Yu and A. Manthiram, "Room-Temperature Sodium–Sulfur Batteries with Liquid-Phase Sodium Polysulfide Catholytes and Binder-Free Multiwall Carbon Nanotube Fabric Electrodes," *The Journal of Physical Chemistry C* 118, no. 40 (2014): 22952–22959, https://doi.org/10.1021/jp507655u.

27. H.-L. Wu, L. A. Huff, and A. A. Gewirth, "Situ Raman Spectroscopy of Sulfur Speciation in Lithium–Sulfur Batteries," *ACS Applied Materials & Interfaces* 7, no. 3 (2015): 1709–1719, https://doi.org/10.1021/am5072942.

28. M. Hagen, P. Schiffels, M. Hammer, et al., "Situ Raman Investigation of Polysulfide Formation in Li-S Cells," *Journal of The Electrochemical Society* 160, no. 8 (2013): A1205, https://doi.org/10.1149/2.045308jes.

29. X. Qu, X. Yu, Y. Liao, et al., "Structural Regulations of Biomass-Derived Hard Carbon for High-Performance Sodium-Ion Batteries," *Journal of Power Sources* 654 (2025): 237786, https://doi.org/10.1016/j.jpowsour.2025.237786.

30. J. Liu, H. Lu, X. Kong, et al., "Formation Mechanism and Molecular Structure of Sulfurized Polyacrylonitrile," *Advanced Materials* 37, no. 29 (2025): 2503534, https://doi.org/10.1002/adma.202503534.

31. H. Zou, Q. Ma, S. Sun, et al., "Nitrogen-Doped Porous Carbon Hosted Sulfur-Rich Polymer for Room Temperature Na-S Batteries with Superior Cycle Performances," *Electrochimica Acta* 486 (2024): 144154, https://doi.org/10.1016/j.electacta.2024.144154.

32. K. N. Wood, E. Kazyak, A. F. Chadwick, et al., "Dendrites and Pits: Untangling the Complex Behavior of Lithium Metal Anodes through Operando Video Microscopy," *ACS Central Science* 2, no. 11 (2016): 790–801, https://doi.org/10.1021/acscentsci.6b00260.

33. G. Li, S. Wang, Y. Zhang, M. Li, Z. Chen, and J. Lu, "Revisiting the Role of Polysulfides in Lithium–Sulfur Batteries," *Advanced Materials* 30, no. 22 (2018): 1705590, https://doi.org/10.1002/adma.201705590.

34. J. Liu, H. Lu, Q. Wang, et al., "Roles of the Polymer Backbone for Sulfurized Polyacrylonitrile Cathodes in Rechargeable Lithium Batteries," *Journal of the American Chemical Society* 147, no. 1 (2025): 426–435, https://doi.org/10.1021/jacs.4c11216.

35. J. Lei, T. Liu, J. Chen, et al., "Exploring and Understanding the Roles of Li_2Sn and the Strategies to beyond Present Li-S Batteries," *Chem* 6, no. 10 (2020): 2533–2557, https://doi.org/10.1016/j.chempr.2020.06.032.

36. A. N. Mistry and P. P. Mukherjee, ""Shuttle" in Polysulfide Shuttle: Friend or Foe?," *The Journal of Physical Chemistry C* 122, no. 42 (2018): 23845–23851, https://doi.org/10.1021/acs.jpcc.8b06077.

37. A. D. Pathak, E. Cha, and W. Choi, "Towards the Commercialization of Li-S Battery: from Lab to Industry," *Energy Storage Materials* 72 (2024): 103711, https://doi.org/10.1016/j.ensm.2024.103711.

38. L. Yin, J. Wang, F. Lin, J. Yang, and Y. Nuli, "Polyacrylonitrile/Graphene Composite as a Precursor to a Sulfur-Based Cathode Material for High-Rate Rechargeable Li–S Batteries," *Energy & Environmental Science* 5, no. 5 (2012): 6966–6972, https://doi.org/10.1039/C2EE03495F.

39. Y. He, S. Bi, C. Jiang, and J. Song, "Recent Progress of Sulfur Cathodes and Other Components for Flexible Lithium–Sulfur Batteries," *Materials Today Sustainability* 19 (2022): 100181, https://doi.org/10.1016/j.mtsust.2022.100181.

40. A. Xu, Z. Jin, B. Wang, et al., "Unraveling the Mechanism on Improved Kinetics Performance of Sulfurized Polyacrylonitrile with Defective Conductive Carbon Matrix," *Chemical Engineering Journal* 484 (2024): 149558, https://doi.org/10.1016/j.cej.2024.149558.

41. M. A. Weret, C.-F. Jeffrey Kuo, T. S. Zeleke, et al., "Mechanistic Understanding of the Sulfurized-Poly(acrylonitrile) Cathode for Lithium-Sulfur Batteries," *Energy Storage Materials* 26 (2020): 483–493, https://doi.org/10.1016/j.ensm.2019.11.022.

42. X. Yu and A. Manthiram, "Capacity Enhancement and Discharge Mechanisms of Room-Temperature Sodium–Sulfur Batteries," *ChemElectroChem* 1, no. 8 (2014): 1275–1280, https://doi.org/10.1002/celc.201402112.

43. L. Fang, W. Xu, X. Lyu, et al., "Suppressing the Shuttle Effects with FeCo/SPAN Cathodes and High-Concentration Electrolytes for High-Performance Lithium–Sulfur Batteries," *ACS Applied Energy Materials* 6, no. 2 (2023): 795–801, https://doi.org/10.1021/acsaem.2c03017.

44. R. Li, Y. Zeng, L. Song, et al., "Mechanism and Solution of Overcharge Effect in Lithium–Sulfur Batteries," *Small* 20, no. 2 (2024): 2305283, https://doi.org/10.1002/smll.202305283.

45. H. Peng, Y. Zhang, Y. Chen, et al., "Reducing Polarization of Lithium-Sulfur Batteries *via* ZnS/Reduced Graphene Oxide Accelerated Lithium Polysulfide Conversion," *Materials Today Energy* 18 (2020): 100519, https://doi.org/10.1016/j.mtener.2020.100519.

46. Y. Wu, Y. Chen, M. Tang, et al., "A Highly Conductive Conjugated Coordination Polymer for Fast-Charge Sodium-Ion Batteries: Reconsidering Its Structures," *Chemical Communications* 55, no. 73 (2019): 10856–10859, https://doi.org/10.1039/C9CC05679C.

47. M. Frey, R. K. Zenn, S. Warneke, et al., "Easily Accessible, Textile Fiber-Based Sulfurized Poly(acrylonitrile) as Li/S Cathode Material: Correlating Electrochemical Performance with Morphology and Structure," *ACS Energy Letters*, 2 (2017): 595–604, https://pubs.acs.org/doi/10.1021/acsenergylett.7b00009?src=getftr&utm_source=sciencedirect_contenthosting&getft_integrator=sciencedirect_contenthosting.

48. Y. Liu, W. Wang, J. Wang, et al., "Sulfur Nanocomposite as a Positive Electrode Material for Rechargeable Potassium–sulfur Batteries," *Chemical Communications* 54, no. 18 (2018): 2288–2291, https://doi.org/10.1039/C7CC09913D.

49. M. Jiang, et al., "Selenium as Extra Binding Site for Sulfur Species in Sulfurized Polyacrylonitrile Cathodes for High Capacity Lithium-Sulfur Batteries," *ChemElectroChem* 6, no. 5 (2019): 1365–1370, https://doi.org/10.1002/celc.201801816.

50. S. Wei, L. Ma, K. E. Hendrickson, Z. Tu, and L. A. Archer, "MetalSulfur Battery Cathodes Based on PANSulfur Composites," *Journal of the American Chemical Society*, 137 (2015): 12143, https://pubs.acs.org/doi/10.1021/jacs.5b08113?src=getftr&utm_source=sciencedirect_contenthosting&getft_integrator=sciencedirect_contenthosting.

51. Y. Sun, X. Wang, A. Yang, et al., "Functional Separator with a Lightweight Carbon-Coating for Stable, High-Capacity Organic Lithium Batteries," *Chemical Engineering Journal* 418 (2021): 129404, https://doi.org/10.1016/j.cej.2021.129404.

52. J. Balach, T. Jaumann, M. Klose, S. Oswald, J. Eckert, and L. Giebeler, "Functional Mesoporous Carbon-Coated Separator for Long-Life, High-Energy Lithium–Sulfur Batteries," *Advanced Functional Materials* 25, no. 33 (2015): 5285–5291, https://doi.org/10.1002/adfm.201502251.

53. H. Li, J. Li, M. Xiang, et al., "A Functional Carbon Decorated Separator for the Confinement and Redox Conversion of Lithium Polysulfides in High Sulfur-Loading Lithium Sulfur Batteries," *Electrochimica Acta* 469 (2023): 143276, https://doi.org/10.1016/j.electacta.2023.143276.

54. X. Lu, G. J. Lian, J. Parker, et al., "Effect of Carbon Blacks on Electrical Conduction and Conductive Binder Domain of Next-Generation Lithium-Ion Batteries," *Journal of Power Sources* 592 (2024): 233916, https://doi.org/10.1016/j.jpowsour.2023.233916.

55. B. Wang, T. Liu, A. Liu, et al., "A Hierarchical Porous C@$LiFePO_4$ /Carbon Nanotubes Microsphere Composite for High-Rate Lithium-Ion Batteries: Combined Experimental and Theoretical Study," *Advanced Energy Materials* 6, no. 16 (2016): 1600426, https://doi.org/10.1002/aenm.201600426.

56. J. Xu, D. Su, W. Zhang, W. Bao, and G. Wang, "A Nitrogen–Sulfur Co-Doped Porous Graphene Matrix as a Sulfur Immobilizer for High Performance Lithium–sulfur Batteries," *Journal of Materials Chemistry A* 4, no. 44 (2016): 17381–17393, https://doi.org/10.1039/C6TA05878G.

57. F. Li, Y. Su, and J. Zhao, "Shuttle Inhibition by Chemical Adsorption of Lithium Polysulfides in B and N Co-Doped Graphene for Li–S Batteries," *Physical Chemistry Chemical Physics* 18, no. 36 (2016): 25241–25248, https://doi.org/10.1039/C6CP04071C.

Supporting Information

Additional supporting information can be found online in the Supporting Information section.

Supporting File: aenm70820-sup-0001-SuppMat.docx.